Nanoscale

Predicting the preferred morphology of hexagonal boron nitride domain structure on nickel from ReaxFF-based molecular dynamics simulations

Journal:	*Nanoscale*
Manuscript ID	NR-ART-12-2018-010291.R1
Article Type:	Paper
Date Submitted by the Author:	17-Feb-2019
Complete List of Authors:	Liu, Song; Kansas State University, Chemical Engineering Comer, Jeffrey; Kansas State University, Anatomy and Physiology van Duin, Adri; The Pennsylvania State University, Mechanical and Nuclear Engineering van Duin, Diana; RxFF_Consulting Liu, Bin; Kansas State University, Chemical Engineering Edgar, Jim; Kansas State University, Department of Chemical Engineering

Nanoscale

ARTICLE

Predicting the preferred morphology of hexagonal boron nitride domain structure on nickel from ReaxFF-based molecular dynamics simulations

Received 00th xxxx 20xx,
Accepted 00th xxxx 20xx

DOI: 10.1039/x0xx00000x

www.rsc.org/

Song Liu,[a] Jeffrey Comer,[b] Adri C.T. van Duin,[c] Diana M. van Duin,[c] Bin Liu*[a] and James H. Edgar*[a]

An understanding of the nucleation and growth of hexagonal boron nitride (hBN) on nickel substrates is essential to its development as a functional material. In particular, fundamental insights into the formation of the hexagonal lattices with alternating boron (B) and nitrogen (N) atoms could be exploited to control hBN lattice morphologies for targeted applications. In this study, the preferred shapes and edge configurations of atomically smooth hBN on Ni(111) were investigated using molecular dynamics (MD) simulations, along with reactive force field (ReaxFF) developed to represent the Ni/B/N system and the lattice-building B-N bond formation. The obtained hBN lattices, from different B:N feed ratios, are able to confirm that hBN domain geometries can indeed be tuned by varying thermodynamic parameters (i.e., chemical potentials of N and B) - a finding that has only been predicted using quantum mechanical theories. Here, we also showed that the nitrogen fed to the system plays a more cruicial role in dictating the size of hBN lattices. With an increase of the relative N content, the simulated hBN domain shapes also transition from equilateral triangles to hexagons, again, consistent with the anticipation based on Density Functional Theory (DFT) calculations. Hence, a plausible approach to acquire a desired hBN nanostructure depends on careful control over the synthesis conditions, which now can benefit from reliable molecular simulations.

Introduction

Hexagonal boron nitride (hBN) has emerged as an important functional material with a characteristic layered lattice composed of an alternating arrangement of boron (B) and nitrogen (N) atoms. As a structural analogue of graphene, the mechanical, thermal, electrical, and chemical properties of hBN, as well as its potential uses, are studied and compared with the well-known carbon-based nanomaterial. hBN is distinguished from graphene by its wide energy band gap (~6.0 eV). Hence, hBN is an excellent electrical insulator for gate dielectrics in electronic device applications.[1] The coupling of hBN and graphene can be exploited to construct heterostructures with tunable electronic properties.[2]

Recently, hBN has shown promise as a functional support to enhance the performance of metal nanocatalysts.[3] While the basal plane of hBN is chemically inert, its edge and defective sites, rich in undercoordinated B and N species, are sufficiently active for selective hydrocarbon oxidative dehydrogenation and CO oxidation reactions.[3, 4]

Growth of 2D or 3D hBN lattice structures with controlled thickness,[5-7] surface area,[7-10] edge orientation,[11] and quality,[12] relies on the understanding of the impact of experimental parameters on synthesis processes. The quality of 3D hBN bulk crystals grown by the metal flux method is sensitive to the choice of the metal and flux system, as well as the temperature and heating and cooling rates of the molten solutions.[6, 7, 13] Bulk crystals – with a domain size of up to 2 mm and thickness of around 200 μm – can be obtained with optimized process parameters. Recently, isotopically enriched hBN crystals have been produced by similar processes using a Ni-Cr flux, and have shown a threefold increase in the phonon polariton lifetime.[14, 15]

The growth of ultrathin hBN structures (consisting of a single atomic layer or a few layers) can be achieved by bottom-up approaches, such as chemical vapour deposition (CVD)[16-29] and molecular beam epitaxy (MBE).[1, 30] Monolayer hBN domains extending to the centimetre-scale have been produced using CVD at atmospheric pressure.[29] Nevertheless, such hBN ultra-thin films are likely polycrystalline, composed of aligned[29] or randomly oriented[20] subdomains on the μm scale. After nucleation, continued growth at the boundaries of the hBN islands leads to coalescence. Depending on the arrangement of B or N atoms at the edges of each hBN domain, the merging of edges with the same terminations prohibits integration via B-N bond formations, thus producing grain boundaries.

The evolution of shape and edge structures of individual hBN domains reveals their growth mechanism. hBN domains commonly exhibit triangular,[20, 26-28] truncated triangular,[16, 26] or hexagonal

[a] Tim Taylor Department of Chemical Engineering, Kansas State University, Manhattan, KS 66506.
[b] Department of Anatomy and Physiology, Kansas State University, Manhattan, KS 66506.
[c] RxFF_Consulting LLC, State College, PA 16801.
† Footnotes relating to the title and/or authors should appear here.
Electronic Supplementary Information (ESI) available: Counts of hexagons in hBN from all MD simulations and DFT-calculated energy energies on Ni(111). See DOI: 10.1039/x0xx00000x

shapes,[10, 26, 31, 32] as determined by their thermodynamic stability on a given substrate. Stehle et al.[26] showed that, on copper foils, the shape of hBN domains is also sensitive to the position of the substrate within the CVD reactor. Specifically, at 1065°C, N-terminated triangular hBN domains formed near the reactor entrance, while the domains tend to have alternating nitrogen and boron-terminations near the reactor exit. The nitrogen source and partial pressure plays an important role in determining crystal shape and sizes as well. Yakobson and co-workers predicted, using density functional theory (DFT) calculations, that the morphology of an hBN monolayer on a nickel substrate can be manipulated by changing from B-rich to N-rich conditions.[33, 34]

hBN domains have a richer variation in morphology than graphene due to their binary composition and lower lattice symmetry.[38] When compared to continuous monolayer hBN sheets, lattices of small hBN fragments are more likely to interact with substrates through their open (growing) edges, although the exact nature of such interaction is debatable. Recently, Zhang *et al*.[35] suggested that better agreement between the experimentally observed and theoretical predicted morphologies is obtained when all edges of the theoretical model are passivated with hydrogen. In experiments, precursor decomposition provides a source for this hydrogen. Regardless, the edge energy plays a critical factor in determining the relative stability and growth mechanism,[34, 36] and the domain shape follows the Wulff principle.[37] Both experiment and theory provided strong evidence that edge structures are influenced by the chemical potentials of its constituents (i.e., μ_B and μ_N). Experimentally, these parameters are typically controlled by synthesis parameters such as the feed compositions of precursors, or nitrogen partial pressure. Theoretically, linear relationships exist between edge energy (γ) and thermodynamic chemical potentials.[33-36, 38] Ultimately, prediction of hBN domain shape and morphology transition can then be realized.

In this work, reactive molecular dynamics simulations supported by the ReaxFF force field, which was specifically developed for the Ni/B/N system,[39] will be used to further reconcile the predicted hBN domain morphologies (currently mainly from DFT calculations) with experimental observations. Here, for the first time, we consider the effect of the B:N ratio on the morphology and edge chemistry of the resulting hBN and, furthermore, determine the thermodynamics of N recombination and its effect on available N for hBN formation. The simulations considered here describe hBN formation in the absence of hydrogen, which is representative of the synthesis of hBN from MBE, in which B powder and N_2 gas are typically used as the B and N sources, and atomic N can be generated by a plasma source.[40-42] Using the B:N ratio as a tunable simulation parameter, mechanistic insights into the formation of different domain shapes and edge terminations will be discussed from analyses of generated molecular trajectories.

Results and discussion

Triangular and hexagonal shaped hBN fragments on Ni(111)

Triangular and hexagonal hBN islands, and semi-periodic ribbons on well-defined single crystal substrates are often used in quantum mechanical calculations to probe the relative stabilities of finite hBN structures consisting of zigzag (B-terminated and N-terminated) and armchair edges.[33-35] Non-periodic, equilateral hBN triangles and hexagons supported on Ni(111), with varying edge lengths (L), were optimized using periodic DFT, as illustrated in Fig. 1 (see Methodology section for computational details). As shown in Fig. 1(a) and 1(b), the designation as B- and N-termination indicates the corresponding outermost atom type. For hexagonal domains, as can be seen in Fig. 1(c), the edges have alternating B- and N-terminations. In all structures, L = *n*, where *n* = 2–5, denotes that there are *n* B–N units on each side. The only exception is the stand-alone hexagonal BN ring, denoted L = 1 and shown in Fig. 1(c).

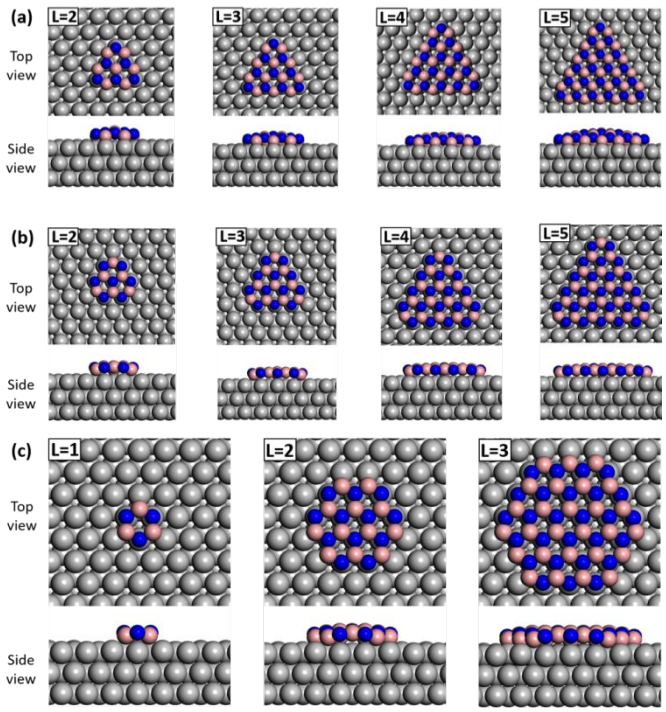

Fig. 1 Optimized triangular hBN domains with (a) B- and (b) N- terminated bare edges with edge length of L = 2–5; and (c) hexagonal domains with bare alternating B- and N-terminated edges with lengths of L = 1–3 on Ni(111). N, B, and Ni are in blue, pink, and gray, respectively.

When supported on Ni(111), nearly all hBN domains are able to maintain lattice structures similar to the bulk without edge passivation, even the smallest domain (L = 1 in Fig. 1(c)). The middle of the hBN domains all protrude slightly while the edge atoms are tightly bound to the Ni surface. This indicates that the binding strength of each hBN island comes from the interaction between the edge atoms (including both B and N) and the surface metal, allowing the interior to detach from the substrate. Specifically, at the edges, on all structures, in Fig. 1(a-c), binding occurs on Ni(111) with N at the top site and B at the 3-fold (hcp or fcc) site. A linear relationship between energy energies of each domain illustrated in Fig. 1 and chemical potential (μ), as reported in the literature,[33] has been established in this work as well (see Figs. S1-3 in ESI). In this work, we aim to examine relationship between hBN monolayer morphology using a developed ReaxFF force field potential,[39] to acquire a physical representation of the influence of chemical potential parameter (μ) from the setting of MD simulations.

ReaxFF MD simulations of hBN growth at different B:N ratios

ReaxFF based classical MD simulations were performed to mimic the hBN MBE process.[40-42] A continuous hexagonal BN lattice from elemental species was attained at the stoichiometric B:N ratio (i.e., 1:1) on Ni(111), as illustrated in Fig. 5(f) in Ref. [39].[39] While the number of deposited B and N atoms will certainly determine the size of the hBN domain, we also anticipate that the availability of B and N will influence the rate of BN lattice formation, as well as the structural quality of the domain, due to diffusion-limited reactions of these building block species.

By setting the number of limiting species (either B or N) to 100, the dependence of hBN growth on the chemical environment can be realized by changing the B:N ratio; values from 3:1 to 1:5 were tested. Hence, compared to the stoichiometric ratio, B:N ratios of 3:1 and 2:1 correspond to B-excess conditions, while other ratios (i.e., 1:2, 1:2.5, 1:3, 1:4, and 1:5) correspond to N-rich conditions.

The hBN domains formed on Ni(111) at 1500 K after 10 ns of simulation with increasing N content are illustrated in Fig. 2 (a–h). Starting with the B-rich scenario, when B atoms significantly outnumbers N atoms (B:N = 3:1), fragmented hBN domains form. These hBN fragments, indicated in black rectangular boxes in Fig. 2(a), consist of BN hexagons joined by their tips or edges. Over the duration of the simulation, each fragment contains no more than six hexagons. The total number of hexagons is no more than 10 as shown in Fig. S4 in ESI. These structures are likely nucleation centres, in which dangling branches abound. Nevertheless, further growth is unlikely because nearly all N atoms are already depleted by forming B-N bonds (with more than one B). All existing fragments are terminated by B. DFT calculations show that B atoms energetically prefer the sublayer of Ni(111).[39] The side view of Fig. 2(a) reveals that the excess B atoms are present throughout the Ni sublayers, and the strong B–Ni bonds severely distorts the substrate lattices causing hBN domains to detach from the substrate. The

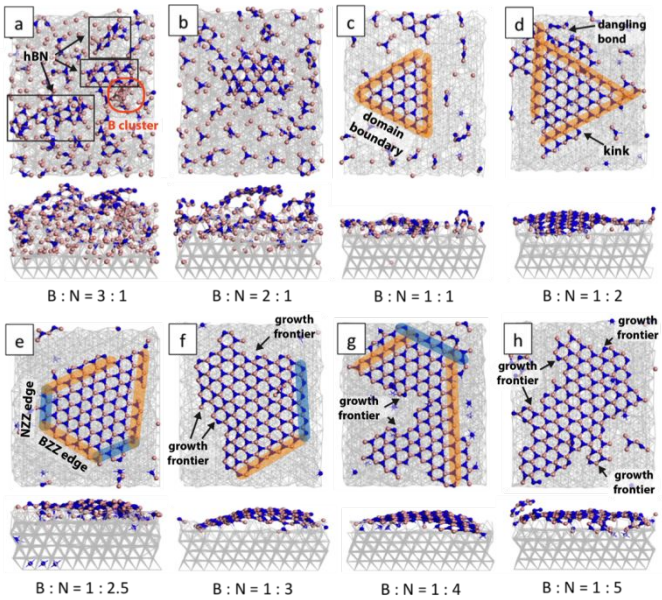

Fig. 2 Images (top and side views) of hBN growth (at 1300K) obtained from MD simulations at 10 ns at B: N ratio of: (a) 3:1, (b) 2:1, (c) 1:1, (d) 1:2, (e) 1:3, and (f) 1:4, respectively. N and B atoms are in blue and pink. The Ni(111) substrate is depicted in grey. B-terminated edges are highlighted in orange; N-terminated edges are blue. B and N zigzag edges are denoted in (e) by BZZ and NZZ, respectively.

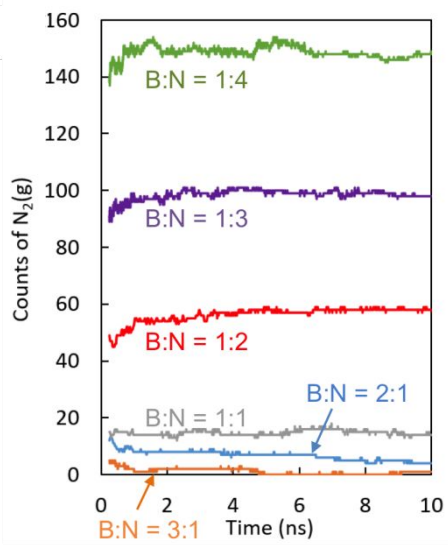

Fig. 3 Numbers of gas phase N_2 molecules, N_2(g), over Ni(111) surface counted over a period of 10 ns of reactive MD simulations at B: N ratios of 3:1 (orange), 2:1 (blue), 1:1 (grey), 1:2 (red), 1:3 (purple), and 1:4 (green).

formation of an all-B cluster (highlighted in the orange circle in Fig. 2(a)) was observed due to the large excess of B atoms that are unable to participate hBN lattice construction. Such B atoms are still abundant on both the surface and in the sublayer, and could enable further growth of B structures.

With a B:N ratio of 2:1, a small hBN island, consisting of approximately 12 BN hexagons with shared edges, assembled, as shown in Fig. 2(b). However, this island is still surrounded by unincorporated N species, mostly bonded with 2–4 B atoms. The level of sublayer B species in excess (i.e., not bonded to N) remains high, although they are now mainly limited within the top two layers (Fig. 2(b) side view). The lattice of the top Ni substrate layer is still highly disrupted.

A small but triangular hBN lattice forms at the stoichiometric 1:1 B:N ratio with 100 N and 100 B atoms. Approximately 20 hBN hexagons were formed (Fig. S4 in ESI). As shown in Fig. 2(c), the resulting structure can be depicted as an equilateral triangle (L = 6) terminated by B on all sides at the zigzag edges (denoted by BZZ and highlighted in orange colour). In addition, a second, but much smaller hBN domain (at the upper substrate boundary of Fig. 2(c)) also formed. Fewer surface-bound N atoms remain on the substrate (the top layer), bounded with 2-3 B atoms. The remaining B species, all surface-bound, are also limited to the top layer. The Ni substrate lattice is relatively intact; it is less distorted than in the B-rich cases. In our previous study, with a larger number of hBN constituent elements (200 B and 200 N atoms), an almost continuous hBN sheet was formed instead,[39] suggesting that the current size is probably limited by the available B and N elements as building blocks, and further growth from these current structures is possible.

When N atoms outnumber B atoms, for instance, in the case of B:N = 1:2 (for 100 B and 200 N atoms), the domain was much larger in area (with L reaching approximately 10 on each side) as seen in Fig. 2(d). This domain structure is anchored on the substrate mainly with its edge sites. The total number of hBN hexagons reaches 30 during the 10 ns simulation. The shape of this domain, which is also bounded mainly by B-terminated zigzag edges (BZZ), approximates

an equilateral triangle. Nevertheless, kinks, dangling bonds, and protruding areas exist, as indicated in Fig. 2(d), and these edge structures can function as growth frontiers. With increasing N content, the number of unincorporated B atoms is further reduced. Few individual B atoms remain on the surface, and even fewer in the sublayer. Also at higher N content, the N species exhibit the ability to *scavenge* B species and facilitate its utilization in hBN lattice construction.

At greater N excess (B:N > 1:2), the morphology of the hBN domains continue to evolve. At B:N = 1:2.5, well-defined N-terminated zigzag (NZZ, highlighted in blue colour in Fig. 2(e)) edges appears. Interestingly, the overall shape of this domain resembles a truncated triangle, with NZZ edges being generated from the truncation of a BZZ triangle. The emergence of NZZ edge signals the transition from B-terminated triangular geometries to other equilibrium morphologies in response to the changing environment as predicted by DFT calculations (Fig. S2 in ESI).[33, 35] DFT-calculated edge energies on Ni(111) based on the hBN domains illustrated in Fig. 1 are also shown as Fig. S3 and Fig. S4 in ESI.

The alternating pattern between BZZ and NZZ becomes even more pronounced at B:N = 1:3. The two highlighted edges are similar in length in the simulation snapshot shown in Fig. 2(f). The hBN domain still grows to a significant extent in terms of the total number of hexagons, which nearly doubles based on 100 B atoms (Fig. S4). As shown in this snapshot, the domain also contains a rather open side, rich in kinks and dangling bonds, as a growth frontier. In this work, further growth along these frontier edges is unlikely because one of the constituent elements, B, is almost completely depleted. Therefore, number of hexagons remains fairly constant under the prescribed simulation condition.

At B:N = 1:4 (Fig. 2(g)), the alternating BZZ and NZZ edges (highlighted) are still recognizable but the simulated domain structure has even more kink sites and dangling bonds. Thus, as the N content (B content fixed) is increased, the hBN domains have the tendency to grow driven by the abundance of N. Adsorption N atoms on Ni(111) without bonding to B, does occur, but is limited by the lack of B. Such a trend continues at the highest N content attempted. At B:N = 1:5, the resulting hBN domain is bounded by growth frontiers on all sides, as shown in Fig. 2(h). In this work, the BN structures produced with excess N are planar and essentially defect free. However, the simulations are limited to relatively small time and length scales. With the demonstrated procedure, the density of defects, particularly if coalescence of multiple hBN nuclei occurred, can be explored with larger simulations.

In this work, the hBN lattice was formed from elemental B and N. Clearly, from Fig. 2(a-h), the constituent species is a critical parameter in determining the equilibrium morphology, including the size, shape, and edge identity, of hBN domains on Ni(111). Excessive B or N will both likely terminate the growth and limit the domain size. Specifically, an adequate supply of elemental N is particularly important for sustained hBN growth. On the other hand, excess elemental B imposes a more significant limitation on hBN lattice formation and is also be disruptive to the integrity of substrate lattice structure that anchors and stabilizes hBN domains during their growth.

Thermodynamics and kinetics of N_2 formation and desorption

In MBE, boron powder and molecular N_2 are generally used as the B and N sources.[40-42] The atomic N can be generated through plasma source, [40] as in eqn. (1), where N^* represents the surface-bound N. Moreover, the thermodynamic cycle between N and N_2 studied in this paper (Fig. S5 in ESI) has shown that $N_2(g)$ can dissociate into N^* to participate hBN growth again.

$$2N^* \leftrightarrow N_2(g) \quad (1)$$

The formation of $N_2(g)$ from N^* according to eqn (1) could compete with the hBN formation process, especially at the initial stage of the MD in which the N concentration is high. However, at high N contents (i.e., B:N = 1:3, 1:4, and 1:5), the fragmentation of hBN domains does not occur is likely because the excess N^* may recombine and desorb from substrate to form $N_2(g)$, according to eqn (1). The counts of $N_2(g)$ at different B:N ratios are shown in Fig. 3 for MD runs over a 10-ns window. At all B:N ratios (even under N lean conditions), $N_2(g)$ exist. At B:N = 3:1 and 2:1, the newly formed N_2 dissociates back into N^*, driven by the excessive B in the substrate available for B-N bond formation. At B:N = 3:1, the amount of $N_2(g)$ (orange) becomes negligible. Similarly, at B:N = 2:1, the amount of $N_2(g)$ (blue) follows a downward trend, decreasing from 15 to 4, and will likely continue to decrease. At the stoichiometric B:N ratio, the $N_2(g)$ count (grey) stabilizes at approximately 18 throughout the MD run, suggesting that an equilibrium is established between $N_2(g)$ and N^* at an early stage. At higher N contents (i.e., B:N = 1:2, 1:3, and 1:4), however, the $N_2(g)$ count in respective case increases within the first 2 ns of MD run before an equilibrium is reached. Once thermodynamic equilibrium is reached, the chemical potential of N is related to that of $N_2(g)$ as $\mu_N = \mu_{N_2(g)}/2$.

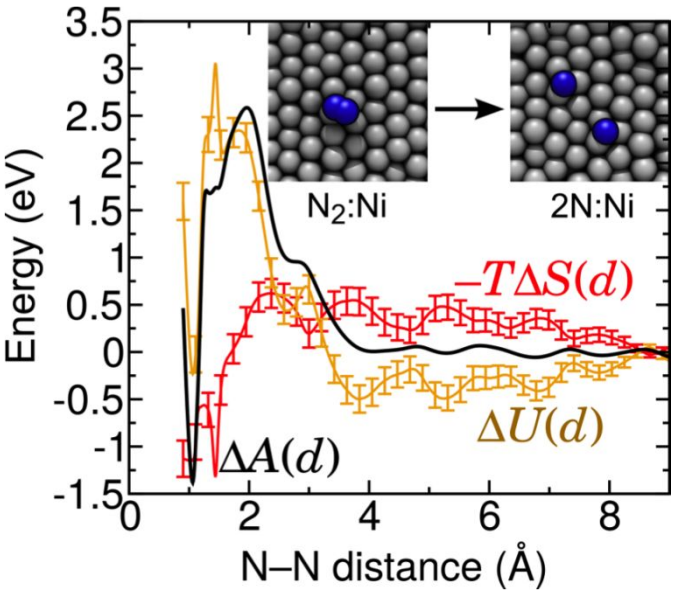

Fig. 4 Free energy profile (black), $A(d)$, for formation of adsorbed N_2 from two N^* on Ni(111), illustrated by the inset figure, in which N and Ni atoms are in blue and grey, respectively. The N-N interatomic distance is used to define the transition coordinate, d (Å). The two separated N* species on Ni(111) at $d > 8$ Å, serves as the zero energy reference. The internal energy (ΔU) and entropic ($-T\Delta S$) contribution to the free energy are also shown in orange and red, respectively. The geometric contribution to the free energy, due to the use of a radial distance coordinate, has been removed to aid interpretation.

To better understand the competition of $N_2(g)$ formation with hBN synthesis, we used an efficient free energy calculation technique (adaptive biasing force) to determine the thermodynamics of $N_2(g)$ formation on Ni(111) based on the ReaxFF potential used in previous MD simulations. The Helmholtz free energy, shown in Fig. 4 (black), was calculated as function of the distance between two N atoms, d (in Å). As is customary, the geometric contribution to the free energy for a spherical radial coordinate ($-k_B T \ln(4\pi d^2)$), has been removed in Fig. 4. This free energy has been also decomposed into internal energy and entropy components, as described in Methodology. As described below, the influence of atomic N on the spatial arrangement of the Ni atoms produces significant entropic effects at the temperature considered (1500 K).

When isolated from one another, the free N atoms are chemisorbed to the Ni(111) surface at the 3-fold sites, respectively (inset figure of Fig. 4). At distances $4\,\text{Å} < d < 8\,\text{Å}$, the force between the two N atoms is essentially zero, where the profile for $\Delta A(d)$ is shown to be flat. However, as the atoms approach each other, certain distances are slightly more favoured than others due to the atomic arrangement of the underneath Ni(111) lattice, leading to appreciable oscillations in the free energy. The reduced spatial freedom of the Ni atoms is reflected in the unfavourable entropy distances of $1.8 < d < 8.2$ Å. The transition from two Ni-bound N atoms to a physisorbed N_2 molecule requires a crossing a large energy barrier at $d = 1.96\,\text{Å}$, which is dominated by the ΔU component ($\Delta U = 2.3 \pm 0.3\,\text{eV}$ at the same d), within reasonable agreement to the energy barrier from DFT calculations (1.7 eV). Once the N atoms are no longer covalently bound to Ni, the freedom of the arrangement of Ni atoms is no longer restricted, and the entropy becomes favourable. The internal energy also becomes favourable with the formation of a stable N_2 molecule. Together, this results in a minimum of the free energy of $\Delta A = -1.38 \pm 0.04$ eV at $= 1.06$ Å.

Once formed, the physisorbed N_2 needs overcome only a small free energy barrier, 0.13±0.03 eV, to desorb from the surface. In comparison, the barrier for desorption of N^* directly from the surface is much larger, requiring 4.47±0.14 eV. Therefore, while excess B at the surface leads to formation of surface-bound B clusters that hinder synthesis of large defect-free hBN domains, formation of N_2 provides a route for more rapid removal of high concentrations of excess N at the surface.

Growth mechanisms of triangular and hexagonal hBN domains

To better understand the differences in hBN lattice formation at different B:N ratios, we analysed slower hBN growth with lower atom concentrations at B:N = 1:1 and 1:3. As discussed in a previous section, equilateral triangular and hexagonal hBN domains were produced, respectively, at these ratios under equilibrium conditions.

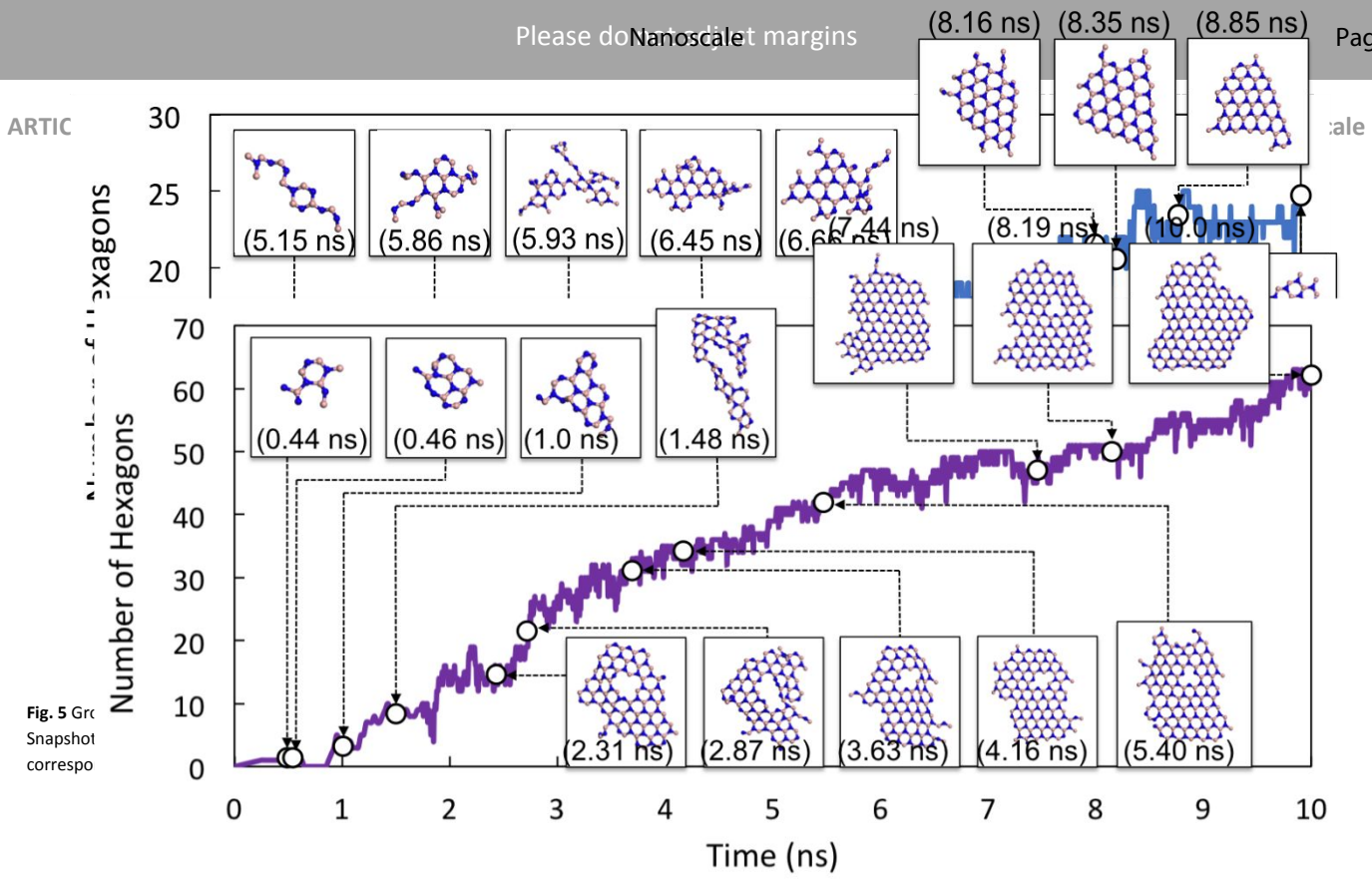

Fig. 6 Growth of hBN domain represented in terms of the count of BN hexagons on Ni(111), shown in purple, at 1300 K and B:N = 1:3 (i.e., 100 B and 300 N). Snapshot images at selected timesteps are shown in boxes, where N and B are shown in blue and pink, respectively. The Ni substrate is omitted for clarity. The timeframes corresponding to each captured image is shown in the parentheses.

With 100 B and 100 N atoms (B:N = 1:1), as depicted in Fig. 5, the first nucleation centre, a BN hexagon ring with branches, appears at 5.15 ns. Then, at 5.86 ns, the structure evolves into a small island consisting of three joint BN hexagons. With these dangling branches, the nucleation centre continues to grow, and at 5.93 ns, the domain size nearly doubled when a second domain, a nucleation centre itself, joined the first domain. In the next 0.5 ns (at 6.45 ns), the hexagon count within the domain increased to 10 hexagons through multiple structural evolutions - via B-N bond formation and chain growth. There are still abundant kink sites and dangling bonds on all sizes of the structure. In the following steps, this hBN domain grows mainly on the upper and lower sides, which are the main growth frontiers in the next 0.9 ns. At 8.16 ns, the right side of the domain has developed into a BZZ edge, while its upper, left, and bottom sides are terminated by –BNB and –NB groups, which will encourage further growth. In the next 1.2 ns, the left and bottom sides of this domain has also developed into the BZZ edge configuration, completing the process of forming a triangular shaped domain bounded by BZZ on all sides (Fig. 2(c)).

For 100 B and 300 N atoms, the nucleation centre was established at 0.44 ns with the formation of the first BN hexagon, as shown in Fig. 6. This growth centre quickly (at 0.46 ns) evolved into a four-hexagon hBN cluster. Note that one heptagon (at the lower left side) with a homoelemental N–N bond was also produced, which is likely at relatively high N contents (≤ B:N = 1:1). At 1.48 ns, a second hBN island joins via the B–N linkage between different domains. This behaviour also occurred at the B:N = 1:1 ratio, suggesting that coalescence can be a common mechanism that accelerate the growth rate. In this case, however, an incomplete vacant area is left at the centre of the hBN domain at 2.31 ns. This reveals a useful clue to understand the origin of potential structural defect - associated with two or more domain structures merge during hBN growth. In this case, the vacant area remained within this domain for over 5 ns before it healed. During this time, its size shrank as it incorporated additional isolated B and N atoms from the Ni substrate. One possible mechanism is that B species in the Ni sublayer may diffuse onto the top layer to access the vacancy. In the last 2 ns, the area was reduced to a single B-vacancy defect. Meanwhile, the outer perimeter of this domain continued to grow and evolve. As shown by the hexagon count (in purple), the number increased by a total of 20 during this period. The additional BN hexagons are mainly added to the left and right sides of the domain structure. At 8.19 ns, the B-point defect was healed; making the entire domain defect-free. Finally, the domain is bounded by BZZ and NZZ edges at the bottom and lower-right sides. The hexagonal-shaped hBN shape is facilitated as the formation of N-terminated edge becomes more thermodynamically favourable, as predicted by DFT calculations (Fig. S3 in ESI).

Conclusions

By combining first-principles calculations and ReaxFF-based MD simulations, the evolution of finite hBN domain morphology and its dependence on the constituent B:N ratio is revealed. The most significant findings can be summarized as follows:

- The morphology, including the size, shape, and edge termination of the simulated hBN domain responds to the variations of the atomic B:N ratio and follows a pattern consistent with earlier predictions from DFT calculations.
- Surplus B species are likely to remain on the top layer and in the sublayer of the Ni substrate. The strong B–Ni interactions severely distort the Ni lattice, and will hinder hBN growth by interfering with its contact with the Ni substrate.

- In contrast, surplus N species will reside on the top layer, but more likely, leave the substrate by forming $N_2(g)$. Once surface-bound N desorbs, a substantial free energy barrier is required for them to dissociate so as to participate hBN growth again. In this regard, N plays a more critical role in controlling the morphology of the hBN domain. In this work, by using elemental B and N directly as sources, larger hBN domains were grown when N was in excess.
- Lastly, the ReaxFF force field, developed from a small set of DFT calculations, is shown capable of describing rather complex behaviours of hBN growth under varying simulated environments. The thermodynamic and kinetic properties predicted from free energy calculations using this force field are gauge well against DFT, suggesting a promising utility to probe more sophisticated processes related to MEB experiments, particularly, in areas of fine-tuning substrate conditions, optimizing experimental temperature, N_2 partial pressure parameters.

Methodology

Models for edge energy calculations on Ni(111)

For finite hBN structures, the chemical bonding at the domain edges, coupled with charge transfer, will dominate the interlayer van der Waals forces between hBN and substrate. Moreover, it has been shown that the edge energies of supported 2-D hBN directly reflect domain's relative stability on a substrate.[18, 43-45] Consequently, the shape and edge of hBN flakes on Cu and Ni follow the Wulff principles.

For edge energy calculations (Figs. S3-S4 in ESI), the nickel substrate for DFT calculations was represented by a 3-layer $p(7 \times 7)$ (111) slab to accommodate hBN domain sizes, yet mitigate the lateral interactions among periodic images. The bottom two layers were fixed at the optimized bulk lattice value (3.52 Å). A vacuum of 30 Å (along the perpendicular direction) was used to separate the top slab layer from the bottom of its own periodic image.

Density Functional Theory (DFT) computational details

Periodic, spin-polarized DFT calculations were employed based on the projector-augmented wave (PAW) method,[46, 47] and the generalized gradient approximation of Perdew-Burke-Ernzerhof (GGA-PBE)[48] functional implemented in the Vienna Ab initio Simulation Package (VASP).[49] Considering the large unit cell, the Kohn-Sham valence states are expanded in a plane-wave basis set up to 350 eV. Only a single gamma point was used to sample the reciprocal Brillouin zone. The Methfessel-Paxton smearing of 0.2 eV was used [50], with the total energies then extrapolated to 0 K. The self-consistent iterations were converged with a criterion of 1×10^{-6} eV, and the ionic steps are converged until the residual force on each atom is less than 0.02 eV/Å.

Molecular Dynamics (MD) simulation setup and procedure

All MD simulations were performed with LAMMPS[51] using the implementation of ReaxFF by Aktulga *et al*.[52] The nickel substrate was modelled using a 5-layer face-centred cubic rectangular slab with exposed (111) facets perpendicular to the z-axis for hBN nucleation and growth. The slab was periodic in the *xy*-plane with 12 × 12 repetition of the unit cell, with a total of 720 Ni atoms. The top four layers were completely unrestrained during the simulations. Harmonic restraints were applied to each atom of the bottom (or the 5th) Ni layer, with a spring constant of 10 kcal mol^{-1} Å^{-1}. There was a vacuum of 90 Å separating successive images along the vertical direction. Initially, the Ni slab was clean.

At the beginning of the simulation, B and N were assigned with random *x*, *y* coordinates in the vacuum above the Ni(111) surface, and then sequentially deposited onto Ni(111) at an interval of 0.25 ps. To prevent premature B–N bond formation, the minimal distance between the initial B and N sources was set to be 1.90 Å, larger than the B–N bond length of 1.44 Å in the hBN lattice. All B and N atoms were deposited on the unrestrained side of the slab, with randomly assigned initial momenta. The same simulation preparation procedure was used for all B:N ratios. All simulations were performed at 1500 K, controlled by the Nosé-Hoover thermostat. The equation of motion was numerically solved using the velocity Verlet integration scheme. Each MD simulation was run for at least 10 ns with a time step of 0.25 fs.

The ReaxFF force field was employed so that chemical processes (e.g., bond formation and cleavage) involving B–N, B–B, N–N pairs and interactions between constituent elements with Ni substrate (e.g., adsorption/desorption, or diffusion) could be fully described. The total potential energy in ReaxFF is formulated as a function of the bond orders of interacting atomic pairs.[53] The ReaxFF force field used was developed for Ni/B/N systems as reported in Ref. [39] (including force field parameters).

Free energy calculations based on MD

Helmholtz free energies (ΔA) were calculated using the adaptive biasing force method,[54, 55] by means of the Colvars module in LAMMPS.[56] The adaptive biasing force method yields $\Delta A(\xi)$, which is the potential of mean force as a function of a transition coordinate (ξ). Because these calculations involved at most two N atoms, it was possible to perform these simulations using a smaller Ni surface model, than the previously described simulations. The slab for the free energy calculation totalled 192 Ni atoms and consisted of three Ni layers. The top two layers of the three-layer slab were completely unrestrained, while a one-dimensional harmonic restraint was applied to each atom of the bottom layer to keep it near the plane $z = -2.05$ Å, using a spring constant of 10 kcal mol^{-1} Å^{-1}. A vacuum of 48 Å separated successive images of the Ni slab along the *z* axis. The periodic slab had dimensions of 18.03×20.81 Å^2 in the *xy*-plane.

For calculations of the $2N \leftrightarrow N_2$ association/dissociation free energies on Ni(111) as well as in vacuum (Calculation 4 in Fig. S5), the transition coordinate was simply the distance between the two free N atoms on the domain $0.90 \leq r_{N-N} \leq 9.00$ Å. Adaptive biasing force bins of 0.01 Å were used to capture the rapid variation of the energy near $r_{N-N} = 1.06$ Å, the equilibrium N–N bond distance for gas phase N_2. In the absence of statistical error, the free energy over a complete cycle would sum to zero. Summing the minimum free energies of Calculations 1–4 yielded a value negligible compared to the magnitude of the free energy changes, −0.06 eV, suggesting that the results had high statistical accuracy.

Each free energy calculation was performed at three different temperatures (i.e., 1200, 1300, or 1400 K) to permit the decomposition of the Helmholtz free energy into entropy and

internal energy using eqns (2-3).[57-59] The temperatures were maintained at the above values by a Langevin thermostat.

$$\Delta S(\xi,T) \approx -\frac{\Delta A(\xi,T+\Delta T/2)-\Delta A(\xi,T-\Delta T/2)}{\Delta T}, \quad (2)$$

$$\Delta U(\xi,T) \approx \Delta A(\xi,T) + T\Delta S(\xi,T). \quad (3)$$

Each simulation was quadruplicated, with different initial velocities and seeds for the Langevin thermostat. A simulated time of 24 ns was obtained for each of the four ReaxFF runs. The mean forces of the four runs were combined, weighting by the sample count, to obtain a potential of mean force representing 96 ns of simulation. The potentials of mean force were anchored according to the convention that the free energy of the dissociated or desorbed state was zero. The statistical uncertainties of the free energies were estimated from the greatest deviation among the four runs, as described Poblete et al.,[60] and propagated through the decomposition into entropy and internal energy.

Conflicts of interest

There are no conflicts of interest to declare.

Acknowledgements

Supports from the Materials Engineering and Processing program of the National Science Foundation, Award number 1538127, and the II-VI Foundation are greatly appreciated. The authors are grateful for the supercomputing support from the Beocat Research Cluster at Kansas State University, which is funded in part by NSF grants CHE-1726332, CNS-1006860, EPS-1006860, and EPS-0919443; and the National Energy Research Scientific Computing Center (NERSC) under the contract No. DE-AC0205CH11231.

References

1. R. Dahal, J. Li, S. Majety, B. N. Pantha, X. K. Cao, J. Y. Lin and H. X. Jiang, *Appl. Phys. Lett.*, 2011, **98**, 211110.
2. A. Ramasubramaniam, D. Naveh and E. Towe, *Nano Lett.*, 2011, **11**, 1070-1075.
3. W. Zhu, Z. Wu, G. S. Foo, X. Gao, M. Zhou, B. Liu, G. M. Veith, P. Wu, K. L. Browning, H. N. Lee, H. Li, S. Dai and H. Zhu, *Nat. Commun.*, 2017, **8**, 15291.
4. J. T. Grant, C. A. Carrero, F. Goeltl, J. Venegas, P. Mueller, S. P. Burt, S. E. Specht, W. P. McDermott, A. Chieregato and I. Hermans, *Science*, 2016, **354**, 1570-1573.
5. C. Zhi, Y. Bando, C. Tang, H. Kuwahara and D. Golberg, *Adv. Mater.*, 2009, **21**, 2889-2893.
6. J. H. Edgar, T. B. Hoffman, B. Clubine, M. Currie, X. Z. Du, J. Y. Lin and H. X. Jiang, *J. Cryst. Growth*, 2014, **403**, 110-113.
7. S. Liu, R. He, Z. Ye, X. Du, J. Lin, H. Jiang, B. Liu and J. H. Edgar, *Cryst. Growth Des.*, 2017, **17**, 4932-4935.
8. C. R. Dean, A. F. Young, I. Meric, C. Lee, L. Wang, S. Sorgenfrei, K. Watanabe, T. Taniguchi, P. Kim, K. L. Shepard and J. Hone, *Nat. Nanotechnol.*, 2010, **5**, 722-726.
9. J. Meng, X. Zhang, Y. Wang, Z. Yin, H. Liu, J. Xia, H. Wang, J. You, P. Jin, D. Wang and X.-M. Meng, *Small*, 2017, **13**, 1604179.
10. R. Y. Tay, X. Wang, S. H. Tsang, G. C. Loh, R. S. Singh, H. Li, G. Mallick and E. H. T. Teo, *J. Mater. Chem. C*, 2014, **2**, 1650-1657.
11. A. Mohsin, N. G. Cross, L. Liu, P. Liu, G. Duscher and G. Gu, *Phys. Status Solidi B*, 2017, **254**, 1700069
12. Y. Kubota, K. Watanabe, O. Tsuda and T. Taniguchi, *Science*, 2007, **317**, 932-934.
13. T. B. Hoffman, B. Clubine, Y. Zhang, K. Snow and J. H. Edgar, *J. Cryst. Growth*, 2014, **393**, 114-118.
14. A. J. Giles, S. Dai, I. Vurgaftman, T. B. Hoffman, S. Liu, L. Lindsay, C. T. Ellis, N. Assefa, I. Chatzakis, T. L. Reinecke, J. G. Tischler, M. M. Fogler, J. H. Edgar, D. N. Basov and J. D. Caldwell, *Nat. Mater.*, 2018, **17**, 134.
15. S. Liu, R. He, L. Xue, J. Li, B. Liu and J. H. Edgar, *Chem. Mater.*, 2018, **30**, 6222-6225.
16. S. Chatterjee, Z. Luo, M. Acerce, D. M. Yates, A. C. Johnson and L. G. Sneddon, *Chem. Mater.*, 2011, **23**, 4414-4416.
17. Y. Kobayashi, T. Nakamura, T. Akasaka, T. Makimoto and N. Matsumoto, *J. Cryst. Growth*, 2007, **298**, 325-327.
18. W. Auwarter, H. U. Suter, H. Sachdev and T. Greber, *Chem. Mater.*, 2004, **16**, 343-345.
19. A. Ismach, H. Chou, D. A. Ferrer, Y. Wu, S. McDonnell, H. C. Floresca, A. Covacevich, C. Pope, R. Piner, M. J. Kim, R. M. Wallace, L. Colombo and R. S. Ruoff, *ACS Nano*, 2012, **6**, 6378-6385.
20. Y.-H. Lee, K.-K. Liu, A.-Y. Lu, C.-Y. Wu, C.-T. Lin, W. Zhang, C.-Y. Su, C.-L. Hsu, T.-W. Lin, K.-H. Wei, Y. Shi and L.-J. Li, *RSC Adv.*, 2012, **2**, 111-115.
21. G. Lu, T. Wu, Q. Yuan, H. Wang, H. Wang, F. Ding, X. Xie and M. Jiang, *Nat. Commun.*, 2015, **6**, 6160
22. N. Guo, J. Wei, L. Fan, Y. Jia, D. Liang, H. Zhu, K. Wang and D. Wu, *Nanotechnology*, 2012, **23**, 415605
23. L. Song, L. Ci, H. Lu, P. B. Sorokin, C. Jin, J. Ni, A. G. Kvashnin, D. G. Kvashnin, J. Lou, B. I. Yakobson and P. M. Ajayan, *Nano Lett.*, 2010, **10**, 3209-3215.
24. Y. Ji, B. Calderon, Y. Han, P. Cueva, N. R. Jungwirth, H. A. Alsalman, J. Hwang, G. D. Fuchs, D. A. Muller and M. G. Spencer, *ACS Nano*, 2017, **11**, 12057-12066.
25. M. P. Levendorf, C.-J. Kim, L. Brown, P. Y. Huang, R. W. Havener, D. A. Muller and J. Park, *Nature*, 2012, **488**, 627.
26. Y. Stehle, H. M. Meyer, R. R. Unocic, M. Kidder, G. Polizos, P. G. Datskos, R. Jackson, S. N. Smirnov and I. V. Vlassiouk, *Chem. Mater.*, 2015, **27**, 8041-8047.
27. K. K. Kim, A. Hsu, X. Jia, S. M. Kim, Y. Shi, M. Hofmann, D. Nezich, J. F. Rodriguez-Nieva, M. Dresselhaus, T. Palacios and J. Kong, *Nano Lett.*, 2012, **12**, 161-166.
28. J. Yin, J. Yu, X. Li, J. Li, J. Zhou, Z. Zhang and W. Guo, *Small*, 2015, **11**, 4497-4502.
29. R. Y. Tay, H. J. Park, G. H. Ryu, D. Tan, S. H. Tsang, H. Li, W. Liu, E. H. T. Teo, Z. Lee, Y. Lifshitz and R. S. Ruoff, *Nanoscale*, 2016, **8**, 2434-2444.
30. T. S. Cheng, A. Summerfield, C. J. Mellor, A. Davies, A. N. Khlobystov, L. Eaves, C. T. Foxon, P. H. Beton and S. V. Novikov, *J. Vac. Sci. Technol. B*, 2018, **36**, 02D103.
31. R. Y. Tay, M. H. Griep, G. Mallick, S. H. Tsang, R. S. Singh, T. Tumlin, E. H. T. Teo and S. P. Karna, *Nano Lett.*, 2014, **14**, 839-846.
32. R. Y. Tay, S. H. Tsang, M. Loeblein, W. L. Chow, G. C. Loh, J.

W. Toh, S. L. Ang and E. H. T. Teo, *Appl. Phys. Lett.*, 2015, **106**, 101901
33. Y. Liu, S. Bhowmick and B. I. Yakobson, *Nano Lett.*, 2011, **11**, 3113-3116.
34. Z. Zhang, Y. Liu, Y. Yang and B. I. Yakobson, *Nano Lett.*, 2016, **16**, 1398-1403.
35. J. Zhang, W. Zhao and J. Zhu, *Nanoscale*, 2018, **10**, 17683-17690.
36. R. Zhao, F. Li, Z. Liu, Z. Liu and F. Ding, *Phys. Chem. Chem. Phys.*, 2015, **17**, 29327-29334.
37. G. Wulff, *Z. Kristallogr. - Cryst. Mater.*, 1901, **34**, 449-530.
38. R. Zhao, J. Gao, Z. Liu and F. Ding, *Nanoscale*, 2015, **7**, 9723-9730.
39. S. Liu, A. C. T. van Duin, D. M. van Duin, B. Liu and J. H. Edgar, *ACS Nano*, 2017, **11**, 3585-3596.
40. A. A. Tonkikh, E. N. Voloshina, P. Werner, H. Blumtritt, B. Senkovskiy, G. Güntherodt, S. S. P. Parkin and Yu. S. Dedkov, *Sci. Reps*., 2016, **6**, 23547.
41. S. Nakhaie, J. M. Wofford, T. Schumann, U. Jahn, M. Ramsteiner, M. Hanke, J. M. J. Lopes and H. Riechert, *Appl. Phys. Lett.*, 2015, **106**, 213108.
42. C. L. Tsai, Y. Kobayashi, T. Akasaka and M. Kasu, *J. Cryst. Growth*, 2009, **311**, 3054-3057.
43. W. Auwarter, M. Muntwiler, J. Osterwalder and T. Greber, *Surf. Sci.*, 2003, **545**, L735-L740.
44. G. B. Grad, P. Blaha, K. Schwarz, W. Auwarter and T. Greber, *Phys. Rev. B*, 2003, **68**, 085404.
45. M. N. Huda and L. Kleinman, *Phys. Rev. B*, 2006, **74**, 075418.
46. P. E. Blochl, *Phys. Rev. B*, 1994, **50**, 17953.
47. G. Kresse and J. Hafner, *Phys. Rev. B*, 1993, **47**, 558.
48. J. P. Perdew, K. Burke and M. Ernzerhof, *Phys. Rev. Lett.*, 1996, **77**, 3865.
49. G. Kresse and J. Furthmüller, *Comput. Mater. Sci.*, 1996, **6**, 15-50.
50. M. Methfessel and A. T. Paxton, *Phys. Rev. B*, 1989, **40**, 3616.
51. S. Plimpton, *J. Comput. Phys.*, 1995, **117**, 1-19.
52. H. M. Aktulga, J. C. Fogarty, S. A. Pandit and A. Y. Grama, *Parallel Comput.*, 2012, **38**, 245-259.
53. A. C. T. van Duin, S. Dasgupta, F. Lorant and W. A. Goddard, *J. Phys. Chem. A*, 2001, **105**, 9396-9409.
54. E. Darve and A. Pohorille, *J. Chem. Phys.*, 2001, **115**, 9169-9183.
55. J. Comer, J. C. Gumbart, J. Hénin, T. Lelièvre, A. Pohorille and C. Chipot, *J. Phys. Chem. B*, 2015, **119**, 1129-1151.
56. G. Fiorin, M. L. Klein and J. Hénin, *Mol. Phys.*, 2013, **111**, 3345-3362.
57. D. E. Smith and A. D. J. Haymet, *J. Chem. Phys.*, 1993, **98**, 6445.
58. S. Wan, R. H. Stote and M. Karplus, *J. Chem. Phys.*, 2004, **121**, 9539-9548.
59. P. Liu, F. Dehez, W. Cai and C. Chipot, *J. Chem. Theory Comput.*, 2012, **8**, 2606-2616.
60. H. Poblete, I. Miranda-Carvajal and J. Comer, *J. Phys. Chem. B*, 2017, **121**, 3895-3907.